

Compression triaxial behavior of concrete: the role of the mesostructure by analysis of X-ray tomographic images

Cedric Poinard^a, Ewa Piotrowska^a, Yann Malecot^{a*}, Laurent Daudeville^a and Eric N. Landis^b

^aUJF-Grenoble 1, Grenoble-INP, CNRS UMR 5521, 3SR Lab, Grenoble, France; ^bThe University of Maine, Orono, ME, USA

This paper is intended to assess the mesostructural damage mechanisms of concrete under hydrostatic and triaxial loadings. Such a study is possible thanks to two state-of-the-art laboratory instruments: a high-pressure triaxial press, and an X-ray computed tomography instrument. The laboratory protocol consists of scanning the concrete prior to the initial loading and after each cycle. An analysis of the resulting images indicates that under high hydrostatic loading, significant damage is visible in cement paste at the mesoscopic scale. For two triaxial tests conducted at 50 and 650 MPa of confining pressure, results reveal major differences in both damage and failure mechanisms. At the lower pressure, shear loading creates a localised failure mechanism characterised by sliding on an inclined plane, whereas at the higher pressure, the strain and damage mode are much more homogeneous with a failure localisation after unloading.

Cet article a pour objectif d'estimer les mécanismes d'endommagement du béton présents à l'échelle mésoscopique sous chargements hydrostatique et triaxial. Une telle étude est possible grâce à deux instruments de laboratoire: une presse triaxiale de grande capacité, et un tomographe à rayons X. Le protocole de réalisation des essais consiste à scanner le béton à l'état vierge et après chaque cycle. L'analyse des images obtenues indique que sous fort chargement hydrostatique, l'endommagement est visible dans la pâte de ciment à l'échelle mésoscopique. Pour deux essais triaxiaux, réalisés à 50 et 650 MPa de pression de confinement, les résultats montrent des mécanismes d'endommagement et de rupture très différents. À basse pression, le cisaillement provoque un mécanisme de rupture qui apparaît sous la forme d'un plan de glissement incliné. À forte pression, la déformation et le mode d'endommagement sont beaucoup plus homogènes avec néanmoins une localisation de la rupture lors de la décharge.

Keywords: concrete; triaxial loading; X-ray tomography; porosity; damage mechanisms

Mots-clés: béton; chargement triaxial; tomographe à rayons X; porosité; mécanismes d'endommagement

1. Introduction

When subjected to a violent explosion or ballistic impact, concrete undergoes very severe triaxial stress states (Zukas et al., 1992). An understanding of concrete behaviour under such loadings requires analysis of the results from triaxial tests that enable

*Corresponding author. Email: yann.malecot@ujf-grenoble.fr

reproduction of the high intensity loading paths. Previous experimental studies have revealed the transition from brittle to ductile behaviour of concrete, as well as the evolution in limit states and the modification of failure patterns with increasing confining pressure (Gabet, Malecot, & Daudeville, 2008; Poinard, Malecot, & Daudeville, 2010; Schmidt, Cazacu, & Green, 2009; Sfer, Carol, Gettu, & Etse, 2002).

Recent experimental and numerical studies (Dupray, Malecot, Daudeville, & Buzaud, 2009; Malecot, Daudeville, Dupray, Poinard, & Buzaud, 2010; Vu, Malecot, Daudeville, & Buzaud, 2009a, 2009b; Vu, Daudeville, & Malecot, 2011) have demonstrated a major influence exerted by the granular skeleton on the concrete response at very high confinement. This behaviour contrasts with the well-known low confinement situations, according to which cement past quality accounts for the main influence on strength.

To expand upon these results, the present paper seeks to offer a better understanding of mesostructural damage mechanisms under both hydrostatic and triaxial loadings. During this research work, two state-of-the-art laboratory instruments have been combined: a high pressure triaxial press capable of introducing 1 GPa confining pressures, and an X-ray computed tomography (CT) device capable of producing 3D images of concrete internal structure at a resolution of near 50 μm . CT has been heavily used over the past few years in the field of materials science and seems to be a very powerful tool for tracking strain localisation in geomaterials (Bentz et al., 2000; Besuelle, 2004; Hall et al., 2010). For cementitious materials, Landis, Zhang, Nagy, Nagy and Franklin (2007) used CT to quantify crack development and damage variables at various cracking levels.

In this experimental study, two concretes are used that only differ by their aggregates shape: crushed aggregate concrete and rolled aggregate concrete. The triaxial compression tests performed on these concretes show that no influence can be ascribed to aggregate shape regarding the triaxial compression response of concrete. As an example, Figure 1 shows the behaviours of rolled and crushed aggregate concretes under triaxial loading at 650 MPa of confining pressure. It appears clearly that the responses are very close. Thus, the damage mechanisms studied in this paper on both concretes will not be greatly affected by the shape difference of aggregates.

The laboratory protocol adopted in this study allows assessment of the damage mechanisms of concrete at the mesoscale. It consists of first conducting a CT scan of an undamaged concrete cylinder and then subsequent scans once the cylinder has been subjected to loading–unloading cycles (§2). Such a protocol reveals the mesostructural

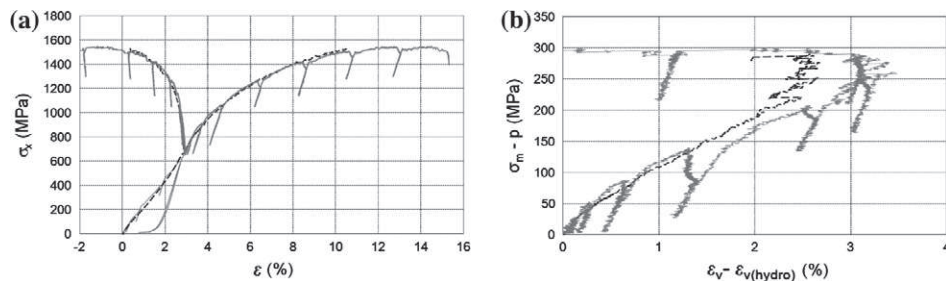


Figure 1. Macroscopic response of concretes during a triaxial compression test at 650 MPa of confining pressure; crushed aggregate concrete (—) and rolled aggregate concrete (- - -). (a) Axial and transverse behaviour; (b) volumetric behaviour in the deviatoric part.

evolution of concrete during these tests. Among other things, damage phenomena are described and the evolution of entrapped porosity is quantified from one cycle to the next (§3). The results of test specimens indicate the strong role played by the largest entrapped pores on hydrostatic behaviour at high confining pressure. The triaxial tests performed at low and high confinements highlight the various damage modes (§4).

2. Experimental set-up

2.1. Concrete samples

In this study, two concrete specimens distinguished solely by their aggregate shape were investigated. The first is a rolled aggregate concrete that has previously been studied by Gabet, Vu, Malecot and Daudeville (2006) and Vu, Malecot and Daudeville (2009). The second specimen is a crushed aggregate concrete. As observed in Table 1, the rolled and crushed aggregates used in these concretes display very similar properties. The mix designs of both concretes, listed in Table 2, were derived in order to obtain two concretes with micro and mesostructure resembling each other as closely as possible.

In this study, we only consider the larger rock pieces as aggregates. The sand used for both concretes is thus the same and has not been taken into account in the term 'aggregate'. Since we are seeking two concretes with the same mesostructure, both test aggregates display the same size distributions. In the crushed aggregate concrete mix design, a small amount of superplasticiser is used instead of a dose of water. This additive adds fluidity to the fresh concrete and thus allows the same slump to be obtained as for the rolled aggregate concrete. We can assume that two concretes with identical slumps also have very close entrapped porosities. This hypothesis appears to be confirmed by the data in Table 2, which presents the experimentally measured porosity values, along with other features relative to both concretes. Figure 2 shows the mesostructure of both concretes. It appears that rolled aggregates make the entrapped porosity more spherical in comparison with the crushed aggregates.

The procedure for preparing these concrete specimens was as follows. After pouring, the concrete blocks were conserved for one month in water and then machined to yield cylindrical specimens 7 cm in diameter and 14 cm long. The next step consisted of drying the specimens at 50°C for at least two months in an oven. Such curing conditions do not dehydrate the cement paste and prevent water from heavily influencing the triaxial compression response as demonstrated by Vu et al. (2009a). Once these two months have elapsed, the concrete saturation level equals approximately 11%, which we will consider as a dry concrete.

The specimen instrumentation consists of just one axial Linear Variable Differential Transformer sensor (LVDT) rather than strain gauges, which create artefacts on CT images of concrete. Such instrumentation does not allow measurement of the circumferential strain of specimens and thus determination of the volumetric behaviour. All speci-

Table 1. Properties of the two types of aggregates used in concrete compositions.

	Crushed aggregates	Rolled aggregates
Percentage of silica	≈ 97	98.7
Density (t m^{-3})	2.6	2.6
Bulk density (t m^{-3})	1.5	1.6

Table 2. Composition and properties of the studied concretes.

Type of aggregate	Rolled (kg m^{-3})	Crushed (kg m^{-3})
0.5/8 'D' gravel	1008	1008
1800 μm 'D' sand	838	838
CEMI52.5NPMESCP2 cement	263	263
Water	169	167.5
Superplasticiser 'Sikafluid'	0	1.8
Density	2278	2278
Property		
Slump (cm)	7	7
Porosity accessible to water ($\pm 0.4\%$)	11.8	10.8
Porosity accessible to mercury ($\pm 1\%$)	12.6	11.9
Entrapped porosity	3.5	3.7
Water/Cement ratio (W/C)	0.64	0.64
Cement paste volume V_p ($\text{m}^3 \text{m}^{-3}$)	0.252	0.25

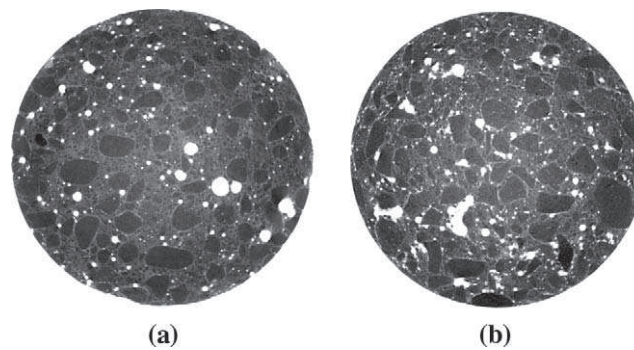


Figure 2. Concrete sample image from a tomographic scan (high density zone in black and low density zone in white). (a) Rolled aggregate concrete; (b) crushed aggregate concrete.

mens undergoing triaxial compression testing are covered with layers of membranes in order to ensure a watertight seal while confining pressure is applied by diethylhexyl azelate, a non-volatile organic liquid, less compressible than water and not self flammable.

2.2. Triaxial press

Specimens were tested on a high-capacity triaxial press capable of generating confining pressures of up to 0.85 GPa and an axial stress reaching 2.3 GPa. A linear position sensor located in the pressure cell is used to control the jack's axial displacement, while a load sensor and pressure sensor also located in the confinement cell indicate the stress state of the sample. The confining pressure and axial displacement of the jack are both servo-controlled, which offers the possibility of creating different loading paths. Additional details on this triaxial press are provided in (Gabet et al., 2006). It has been shown that the friction effect at the specimen ends can be neglected during triaxial tests with high confinement.

2.3. Tests

In this paper, only triaxial compression tests are presented. Such tests begin by applying a hydrostatic load up to the intended confining pressure; next, while holding lateral stress constant, the specimen is axially loaded (see Figure 3). The triaxial press employed allows application of cycles during the hydrostatic part or the deviatoric part of the test.

The degradation mechanisms of concrete are investigated by performing a succession of loading–complete unloading triaxial compression cycles. Furthermore, after each unloading, the specimen is removed from the press and scanned with its membrane layers serving as protection.

In this work, compressive stresses and contraction strains are defined to be positive: σ_x is the principal axial stress, p the pressure inside the confining cell, σ_m the mean stress (Equation (1)), and q the principal stress difference (i.e. deviatoric stress):

$$\sigma_m = \frac{\sigma_x + 2 \cdot p}{3} \quad (1)$$

Considering the important strain of concrete under compression triaxial tests, a large strain description is used in all the tests presented in this paper. On the other hand, the computation of the true axial stress (taking into account the evolution of diameter) is impossible if the circumferential strain is not measured.

The various tests presented in this paper are described in Table 3. Two specimens, each one representing a type of concrete, underwent a triaxial test at 650 MPa of confining pressure with loading–complete unloading cycles in the hydrostatic part and in the deviatoric part. Two other specimens, again one of each studied concrete, were subjected to triaxial tests at 50 MPa of confinement with cycles only in the deviatoric part.

2.4. The CT machine

This multi-scale X-ray tomograph allows study of the *in situ* behaviour of geomaterials such as sandstone (Charalampidou, Hall, Stanchits, Lewis, & Viggiani, 2011), mortar (Landis et al., 2007) and concrete (Wong & Chau, 2005). This innovative device was designed and manufactured by the RX Solutions company (RX Solutions SARL, Chavanod, France) and is able to scan objects whose diameters vary from 4 mm to 200 mm with resolutions of 5 and 100 μm , respectively.

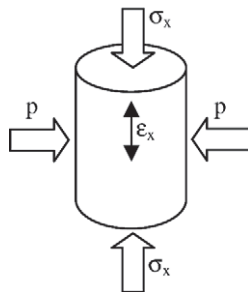


Figure 3. Diagram depicting stresses and the measured strain on the sample.

Table 3. Tested specimens under triaxial loading cycles and tomographic scans.

Specimen designation	Type of concrete	Hydrostatic cycles (MPa)	Triaxial cycles	Number of scans
R650	Rolled aggregate	3 cycles 200; 400; 650	1 cycle at 650 MPa of confinement	5
R50	Rolled aggregate	None	3 cycles at 50 MPa of confinement	4
C650	Crushed aggregate	3 cycles 200; 400; 650	3 cycles at 650 MPa of confinement	7
C50	Crushed aggregate	None	2 cycles at 50 MPa of confinement	3

X-ray CT is a non-destructive imaging technique that enables characterisation of the 3D structure of materials; its results provide a set of images with voxel (three-dimensional pixel) values representing an approximation of the local density of the material. It then becomes possible to observe the meso or microstructure of the scanned object. First, the sample scan yields radiographies to represent the X-ray mass attenuation. The Beer–Lambert Law (Equation (2)) introduces a set of parameters that depend on X-ray attenuation, such as material thickness and the linear coefficient of attenuation:

$$I = I_0 \cdot \exp\left(-\int \mu(x)dx\right) \quad (2)$$

where I_0 = number of photons emitted by the source; I = number of photons passing over the studied object; and $\int \mu(x)dx$ = global linear coefficient of attenuation of the thickness of material crossed by the X-ray.

A mathematical algorithm, called filtered back projection, then derives the linear coefficient of attenuation μ in each pixel of the horizontal slices (CT images) of the scanned zone. Since this parameter is related to mass density, each voxel has a value close to the average mass density of components existing in the voxel.

For this paper, the laboratory protocol consists of first conducting a CT scan of an undamaged concrete cylinder and then subsequent scans once the cylinder has been subjected to loading–unloading cycles. This method serves to monitor the mesostructural evolution of concrete during a triaxial compression test in spite of the inevitable unloading that occurs before the scan.

CT parameters need to be chosen for the scans. They will be the same for all the scans. The tension is equal to 150 kV, which is the maximum of the CT machine. Such a high value is necessary due to both density and thickness of the concrete specimen. The intensity is equal to 400 μ A with an exposure time of 0.1 s. In order to restrict the noise of CT images, we use an average of 40 images to obtain each of the 1200 radiographies. Using these parameters leads to a scanning time equal to 2 hours.

The repeatability of CT images has never been studied. Nevertheless, the scan parameters are identical and a system is used to centre the specimen on a plate, making sure the resolution doesn't change from one scan to another. In addition, both porosity and diameter of a specimen scanned twice (undamaged and very slightly damage at the mesoscale) are quasi identical (see section 4.2.2).

3. Image analysis techniques

The CT images (Figure 4) have a resolution of 52 μm . This value comes from the pixel size of the detector and the positioning of the specimen between the X-ray source and the detector. The latter is in order to zoom as much as possible on the specimen but making sure all the diameter is scanned. Then, the size of the scanned zone is roughly equal to 6 cm high by 8 cm wide.

The resolution of these CT images is sufficient to comprehend the mechanisms existing at the mesoscopic scale (aggregate size) and then to associate them with macroscopic behaviour. These images require processing to reveal the mesostructure and quantify the modifications. This part of the paper is aimed at presenting the image analysis techniques applied to the CT images of all scanned zones.

3.1. Observation of damage and localised mechanisms

Since numerous scans are performed on each specimen at different states, one easy way to evaluate damage consists of comparing slices of the same part of the sample. Currently, these same slices coming from two different volumes are visually identified. The CT images obtained from a scan do not depict the mesostructure very accurately, making modifications necessary in order to improve the quality of visual images. This process, which is automatic, simply entails modifying both the contrast and luminance in a way that allows focus solely to be on the grey level corresponding to the concrete mesostructure. Nevertheless, these grey levels are chosen 'by eye' from the grey-level histogram. Figure 4 shows the same horizontal slice before and after processing; in Figure 4 (b) the membranes are no longer present and the various concrete elements are more easily visible. The lowest grey level (black) corresponds to the least dense zones while the highest level reflects the densest zones. The images of all scans will be modified with this process.

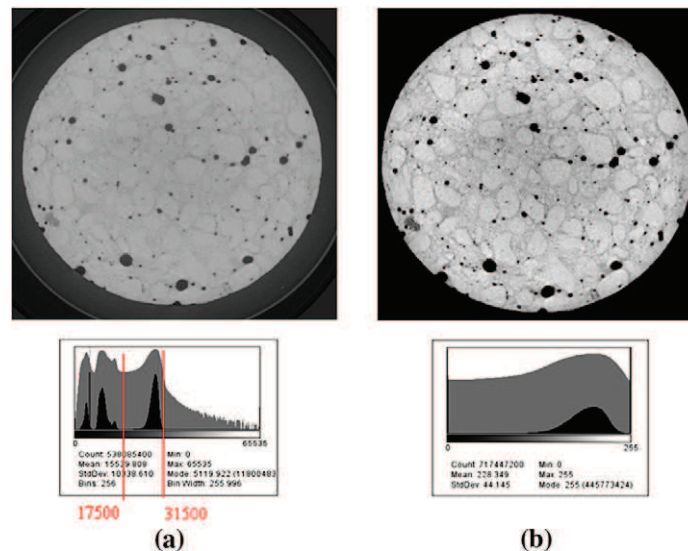


Figure 4. Horizontal slice of rolled aggregate concrete specimen with the grey level histogram: (a) before modification; (b) after modification of both contrast and luminance.

3.2. Damage mechanism assessment

Concrete porosity depends not only on many choices made during the concrete formulation, but also on the actual concrete pouring technique employed. The three pore classes existing in cement are gel porosity ($< 3 \text{ nm}$), capillary porosity ($< 10 \text{ }\mu\text{m}$), and the entrapped air porosity created during concrete pouring. The spherical shape and mean dimension around one millimetre make this latter identifiable with CT images (Figure 4).

3.2.1. Porosity segmentation

Entrapped porosity is the only type of porosity that can be identified on CT images. The image processing approach, called segmentation, presented in this section is intended to describe the various steps conducted to isolate both porosity and diameter of the scanned specimens. This image processing technique has been developed by Eric Landis and his team (Landis et al., 2007) to study the behaviour of mortar, and was adapted for the purposes of this study. The segmentation process is not a new technique and has already attracted the interest of many authors (Werner & Lange, 1999; Yang & Buenfeld, 2001). One feature characterising such a processing approach is the lack of a single true result, but instead a number of results that depend on parameter choices. The result of segmenting the entrapped porosity then depends solely on the choice of grey level that differentiates the matter from voids. Since there is an uncertainty on this grey level, it is identified to provide a segmented porosity of the undamaged concrete equal to the entrapped porosity measured experimentally (3.5%). Figure 4(a) displays a horizontal slice and the associated grey-level histogram. It appears that the grey level equal to 17,500 yields an entrapped porosity (with an analysis of 1000 slices) of 3.5%, which is an average of four undamaged scanned specimens. This grey level was then used to segment both porosity and diameter on all scans, even for the damaged specimens.

The segmentation steps for porosity are presented in Figure 5 for one horizontal slice. The first step (threshold, Figures 5(a) and 5(b)) uses the grey level of 17,500 as a threshold to separate pixels into two classes: those less than this grey-level threshold are assigned a zero value (black pixels), while all others are assigned a 1 value (white). The second step (boundary detection, Figure 5(c)) consists of detecting the cylindrical outline of the slice ('boundary detection' step) by isolating the largest pore from the previous image. As a final step (image combination, Figure 5(d)), the two last images are combined to provide only the pores. This image processing sequence has been applied to all horizontal slices obtained from a given tomographic scan. It can be performed slice by slice or directly on the whole volume.

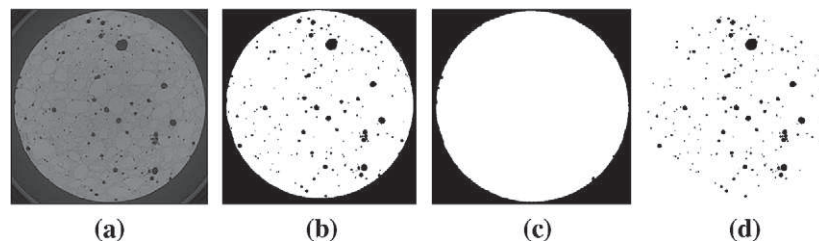


Figure 5. Porosity segmentation process steps: (a) original CT image; (b) threshold; (c) boundary detection; (d) image combination.

3.2.2. Segmentation results

The results of these segmentation steps allow assessment of an array of features. We already mentioned the entrapped porosity computed by dividing the voxels corresponding to the pores (Figure 5(d)) with voxels corresponding to the specimen (Figure 5(c)). In addition, since a CT scan generates many horizontal slices, it is also possible to plot both curves depicting entrapped porosity and diameter in the height of the specimen (X-direction). To compute the diameter, the white area of the contour image (Figure 5 (c)) is assumed to be the area of a disk.

The outline images are also helpful in assessing the inelastic volumetric strain of the test concrete specimen. Such an assessment may be performed by determining the volume of the concrete specimen at different states (Figure 6). This method is actually quite straightforward since it merely involves finding the first and last slices defining the same concrete part limits for the undamaged sample and after each cycle. The inelastic volumetric strain obtained from this method has a maximal relative error of $\pm 25\%$ given that the first and last slices have been visually identified. This uncertainty on the inelastic volumetric strain comes directly from the relative error on Δh (the decrease in the number of slices) in the computing of the inelastic axial strain (Equation (3)). Due to the fact that a horizontal slice does not remain horizontal under loading, the error of Δh and so of the inelastic volumetric strain can be up to 25%.

$$\varepsilon_x = \frac{\Delta h}{h} \quad (3)$$

Image correlation enable strain within volume images to be obtained more precisely, as is shown by Bay, Smith, Fyhrie and Saad (1999) and Limodin et al. (2010). However, this technique does not provide relevant results on our CT images due to the fact that, in most cases, the mesostructure changes too much from one scan to another.

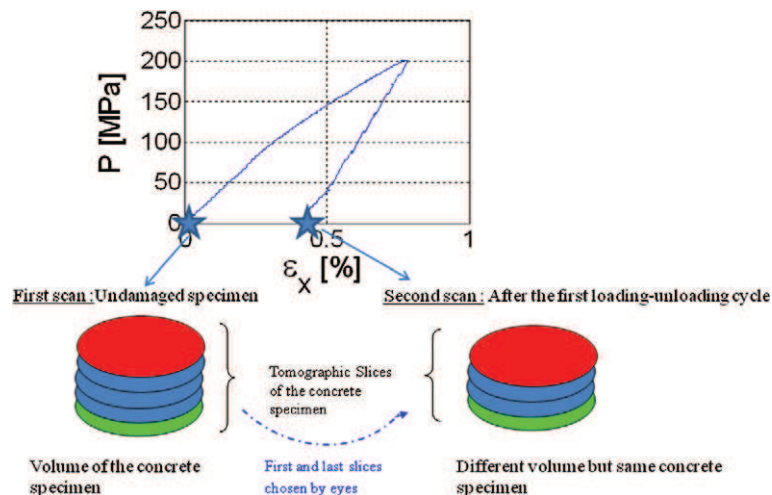


Figure 6. Diagram representing the segmentation process for assessing the inelastic volumetric strain with tomographic images of a concrete specimen.

4. Damage mechanisms of concrete examined under triaxial compression testing

The image analysis technique presented in §3 is now used to better understand concrete behaviour under both hydrostatic loading and triaxial compression loading at low and high confining pressures.

4.1. Hydrostatic test up to 650 MPa

The results of both specimens, R650 and C650, subjected to cyclic hydrostatic loadings prove to be similar in terms of macroscopic behaviour and mesostructural evolution. Only the results from the rolled aggregate concrete specimen will thus be presented. Figure 7 shows the volumetric behaviour under hydrostatic loading where the volumetric strain is assumed to be equal to three times the axial strain.

For this experimental series, the specimens' caps were removed to allow for scanning after each cycle. The extra handling causes the reloading to be less steep than unloading due to the additional crushing of concrete–cap interfaces. In order to derive a consistent behaviour, each reloading has been fitted onto the previous unloading. The hydrostatic loading cycles up to 650 MPa of confining pressure illustrate the main features of classical hydrostatic tests on concrete. The upper envelope of the volumetric behaviour curve indicates a major modification in the tangent bulk modulus of concrete. A decrease is visible from 80 MPa to 250 MPa, after which the concrete tightens. The unloading–reloading cycles are steeper than the upper envelope due to the absence of an irreversible mechanism during these cycles. As explained previously, the reloading steps have been fitted onto the unloads to the maximum loading level reached during the previous cycle. The concrete specimen response then follows the curve obtained without any intermediate unloading–reloading. The elastic bulk modulus, as determined by the linear part of the hydrostatic unload, increases slightly with confining pressure. This modification, which is significant at low pressure and very weak beyond, is similar to what was observed during a cyclic hydrostatic test on the same material (Poinard et al., 2010).

Figure 8 shows the same horizontal slice of the R650 specimen in the undamaged state (a) and after each hydrostatic cycle (b, c, d). These images show that concrete compaction is significant at the mesoscale for pressures above 200 MPa. After the first cycle, no damage is visible and moreover the quantitative measurements do not change

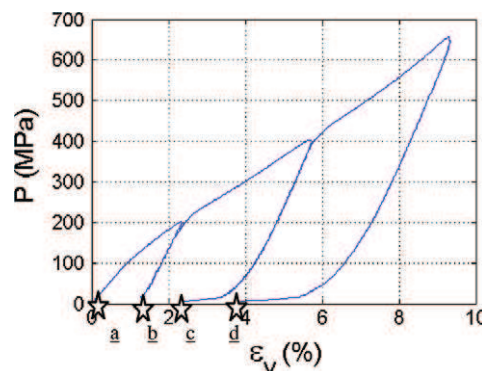


Figure 7. Volumetric behaviour of the R650 specimen under hydrostatic loading–unloading cycles up to 650 MPa of pressure with scans: (a) undamaged; and (b), (c), (d) after each cycle.

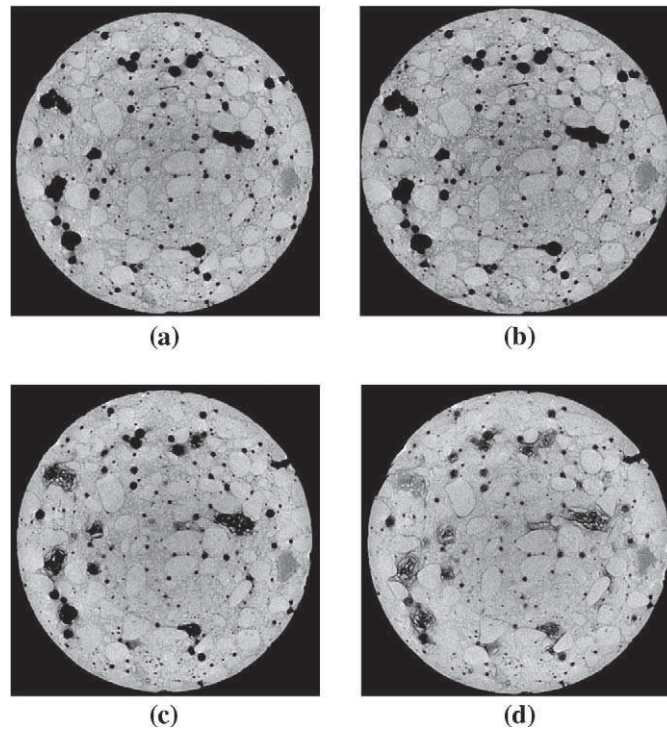


Figure 8. Horizontal slice of R650 specimen after increasing hydrostatic cycle (load-unload): (a) undamaged; (b) after 200 MPa; (c) after 400 MPa; and (d) after 650 MPa.

significantly. The left-hand side of Figure 9 displays a very slight drop in entrapped porosity with the first cycle, while the size distribution for this type of pore remains unchanged (Figure 10). The porosity closure mechanisms however have already been initiated, as the inelastic volumetric strain equals 1.1% and the diameter decrease is significant (see Figure 9(b)). The first cycle actually compacts the concrete specimen at the

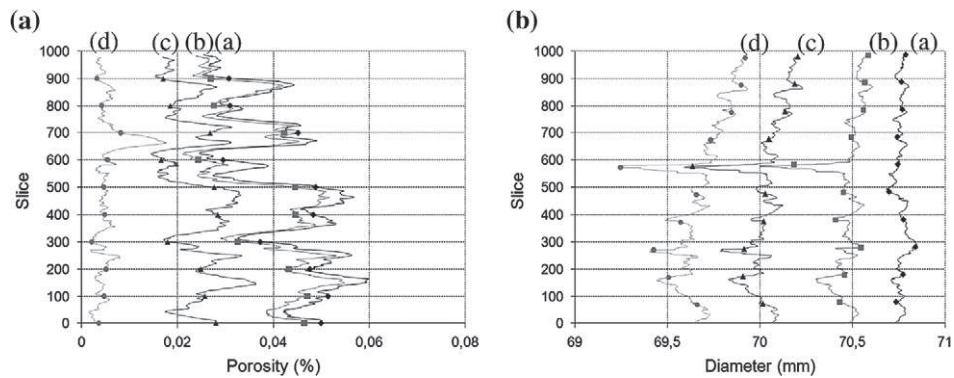


Figure 9. Porosity and diameter of R650 specimen after increasing hydrostatic cycles: ♦ undamaged; ■ after 200 MPa; ▲ after 400 MPa; ● after 650 MPa. (a) Entrained porosity in the X-direction; (b) diameter in the X-direction.

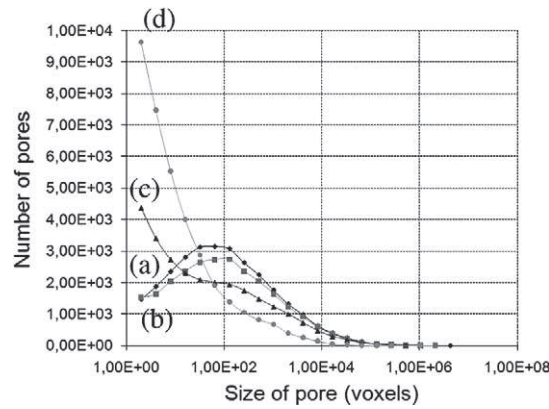


Figure 10. Size distribution of entrapped porosity of R650 specimen after increasing hydrostatic cycles: \blacklozenge undamaged; \blacksquare after 200 MPa; \blacktriangle after 400 MPa; \bullet after 650 MPa.

microscale, as indicated in Figure 11. The inelastic volumetric strain is almost three times greater than the loss of entrapped porosity.

The subsequent cycle up to 400 MPa of confinement leads to real mesostructural damage. The filling of large pores with debris causes thin cracks opening in the matrix (Figure 8). The collapse of the largest pores during this second cycle appears very clearly in Figure 10; the number of large pores decreases while the number of small pores rises considerably. These aggregates also exhibit signs of damage near the large pores; some of them are cracked and others have become unbonded (Figure 8). For this second cycle, Figure 9 indicates a major decrease in entrapped porosity, especially over the bottom part. The zones of highest porosity start to collapse first. It is also worth noting that this drop in entrapped porosity is as strong as the increase in inelastic volumetric strain for this second cycle (Figure 11). At this stage, damage is present at the mesoscale.

This mesostructural damage grows, over the entire scanned zone, during the last hydrostatic cycle up to a pressure of 650 MPa. The entrapped porosity decreases and

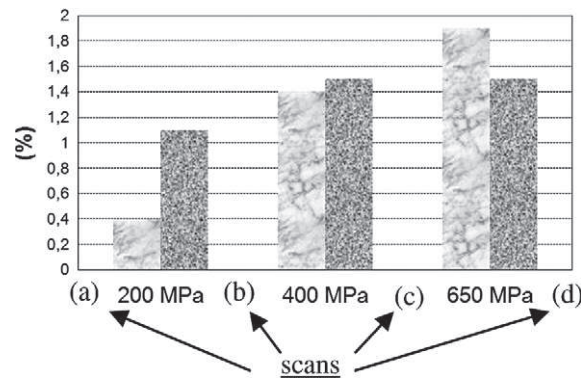


Figure 11. Comparison between the incremental increase in inelastic volumetric strain \blacksquare and the incremental drop in entrapped porosity \square of the R650 specimen over the course of hydrostatic cycles.

becomes much more homogeneous (Figure 9). The only peak that remains corresponds to a piece of the membrane stuck inside a large pore close to the surface. The more sizable decrease in diameter over the bottom part is due to strong compaction of the high-porosity zone. This last cycle produces an outstanding feature, namely a more pronounced drop in entrapped porosity than the corresponding increase in inelastic volumetric strain (Figure 11). This phenomenon might be explained by a significant loss of cohesion that leads to microcracks opening during unloading, which is not captured by the tomographic images.

In conclusion, this cyclic hydrostatic test shows significant modification of the mesostructure for pressures above 200 MPa. Beyond this threshold, collapse of the largest entrapped pores facilitates damage growth, which diminishes concrete cohesion. Thin cracks start to appear in the aggregates and cement matrix at the mesoscale.

4.2. Triaxial tests

4.2.1. Triaxial test at 650 MPa of confining pressure

After a series of cyclic hydrostatic loadings, the R650 and C650 specimens were subjected to triaxial compression loadings at a confining pressure of 650 MPa. The R650 specimen only underwent one loading–unloading cycle in order to reach rupture, whereas three increasing loading–unloading cycles were applied to the C650 specimen. To observe the mesostructural evolution of concrete with axial compression at a very high confining pressure, the results of the C650 specimen will now be presented with special attention paid to the last three cycles. Figure 12 displays the axial response of this specimen subjected to the cyclic triaxial test at 650 MPa of confining pressure. The hydrostatic part of the test displays the same properties as the ones explained in the previous section. The upper envelope of the deviatoric part shows a progressive decrease in the tangent Young's modulus. A triaxial test at such confining pressure creates the arrival at the strain limit state, defined by the contractancy–dilatancy transition on the volumetric behaviour curve, while the stress is still increasing. Even at the end of the axial compression the stress peak is not reached. Like for the previous specimen

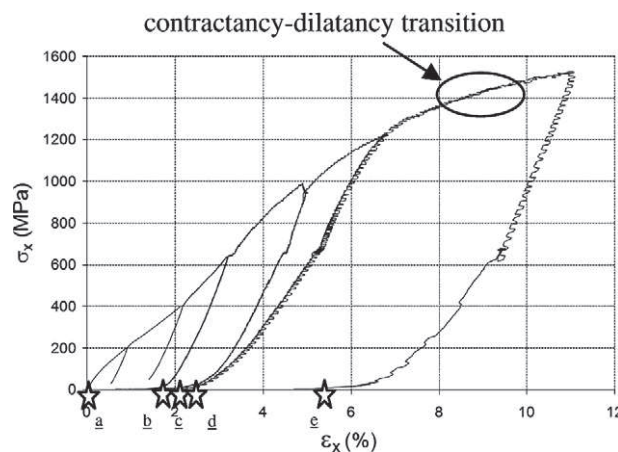


Figure 12. Axial behaviour of C650 specimen under triaxial test at 650 MPa of confining pressure and the studied scans: (a) undamaged; and (b), (c), (d), (e) after different cycles.

tested, the reloads were fitted onto the unloads, except at the end of the penultimate cycle, at which time a problem with the LVDT sensor led to reloading of the last cycle. The final two cycles were performed in order to scan the specimen before and after the contractancy–dilatancy transition. Since concrete has a reproducible behaviour, we used other triaxial tests at 650 MPa of confining pressure, performed on specimens with a complete instrumentation (axial and circumferential gages), to determine when the cycles had to be performed.

Figure 13 shows the mesostructure of the C650 specimen at various steps: undamaged, after the 650 MPa hydrostatic cycle, and after the first, second and third triaxial cycles in the deviatoric part of the test. These images clearly suggest the strong compaction of concrete with axial compression at very high confining pressures. The increase in grey levels within the cement matrix also highlights the material densification due to porosity collapse. Damage phenomena spread tremendously as the triaxial cycles progress, with thin cracks appearing in the cement matrix and the majority of aggregates becoming unbonded and cracked.

The quantitative measurements provide an effective illustration of mesostructural evolution in the C650 specimen. With the first triaxial compression cycle in the devia-

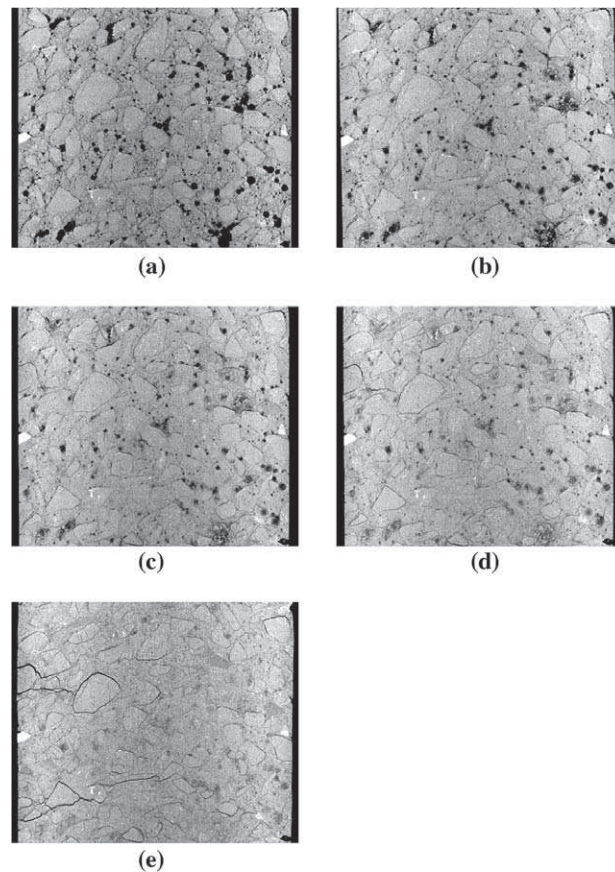


Figure 13. Vertical slice of the C650 specimen after triaxial cycles: (a) undamaged; (b) after hydrostatic cycle at 650 MPa; and after the (c) first, (d) second and (e) last cycles in the deviatoric part of the triaxial test at 650 MPa of confinement.

toric part, both entrapped porosity and diameter in the X-direction decrease, yet this trend ceases with the second cycle (Figure 14). The absence of diametric evolution with the second cycle, whereas the inelastic volumetric strain (Figure 15) continues to increase, is explained by the strong concrete compaction in the X-direction. During the third (last) triaxial compression cycle, a maximum compaction state is reached which leads to a strong increase in specimen diameter over the entire scanned zone height; this phenomenon gives rise to the contractancy–dilatancy transition observed on the volumetric behaviour curve.

The rearrangement is so extensive with the last compression cycle that concrete cohesion becomes very low. The unloading then triggers the opening of cracks, perpendicular to the axial direction, at the mesoscale (Figure 13(e)) and thus an increase of the entrapped porosity. This last feature is shown by the third cycle in Figure 15, which shows a negative incremental porosity drop. The evolution in concrete particle size distribution with triaxial cycle is displayed in Figure 16, which very accurately depicts the severity of the air bubble porosity collapse.

The R650 (rolled aggregate concrete) specimen was also subjected to one triaxial cycle at 650 MPa of confinement up to the contractancy–dilatancy transition. The scan performed after this cycle shows an outstanding failure pattern: a large crack almost perpendicular to the axial compression direction has actually cut the specimen into two parts. Figure 17 exhibits a vertical slice of the R650 specimen at the various states: undamaged, after a hydrostatic loading–unloading cycle at 650 MPa, and after the triaxial loading cycle up to the failure. It is worth noting that this crack avoids the aggregates. An observation of images representing the mesostructure also reveals other small cracks very close to this large one. The mesostructural quantitative measurements of this specimen show the same modifications as for the C650 specimen. The diameter increases over the entire scanned zone, while entrapped porosity remains near 0 (except in the crack zone). Both the C650 and R650 specimens present a similar failure pattern

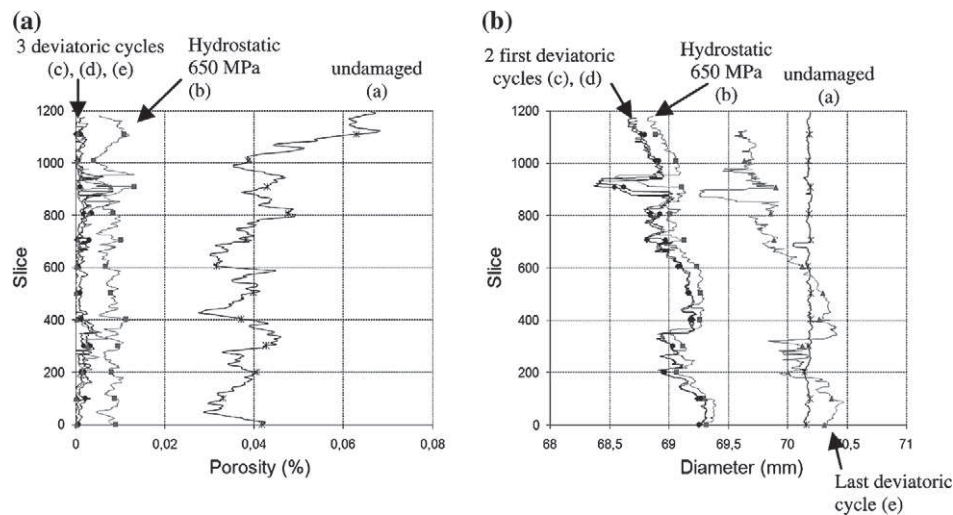


Figure 14. Porosity and diameter of C650 specimen after increasing loading cycles: \times undamaged; \blacksquare hydrostatic at 650 MPa; and \bullet first, \blacklozenge second and \blacktriangle last cycles in the deviatoric part of the triaxial test at 650 MPa of confinement. (a) Entrapped porosity in the X-direction; (b) diameter in the X-direction.

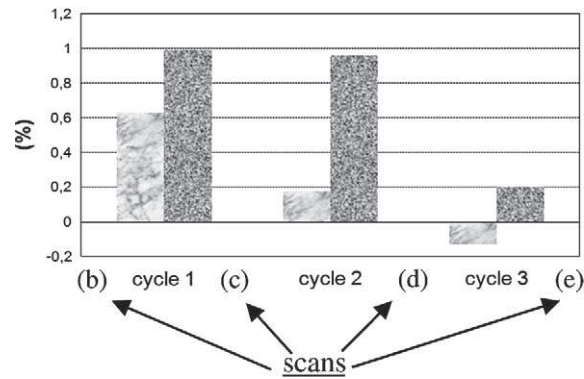

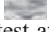


Figure 15. Comparison between the incremental increase in inelastic volumetric strain  and the incremental drop in entrapped porosity  of the C650 specimen over the course of loading cycles in the deviatoric part of the triaxial test at 650 MPa of confinement.

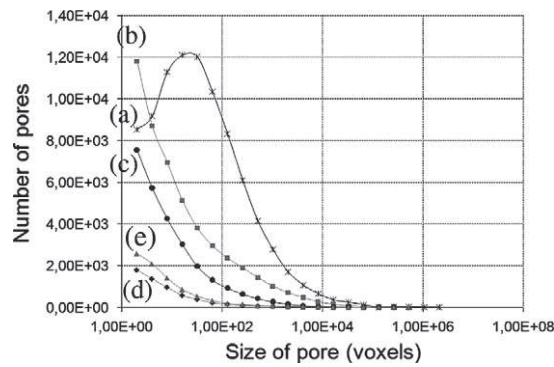


Figure 16. Size distribution of entrapped porosity of the C650 specimen after increasing loading cycles: \times undamaged; \blacksquare hydrostatic at 650 MPa; and \bullet first, \blacklozenge second and \blacktriangle last cycles in the deviatoric part of the triaxial test at 650 MPa of confinement.

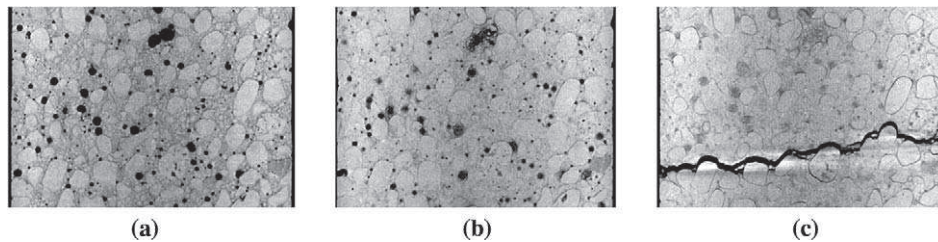


Figure 17. Vertical slice of R650 specimen after triaxial loading cycles: (a) undamaged; (b) after the hydrostatic cycle at 650 MPa; and (c) after the triaxial cycle at 650 MPa of confinement up to the failure.

with strong compaction and rupture localisation. This last feature, which appears in the crack shape perpendicular to the axial compression, is more pronounced for the R650 specimen.

All the triaxial tests performed at very high confining pressure up to the contractancy–dilatancy transition show at least one horizontal band. This failure localisation contrasts with the diffuse damage mechanisms leading to strong concrete compaction.

4.2.2. Triaxial test at 50 MPa of confining pressure

Figure 18 provides the axial stress–axial strain curve of the R50 specimen subjected to three triaxial compression cycles at 50 MPa of confining pressure. The hydrostatic compression shows a linear elastic behaviour, while the upper envelope of the deviatoric part shows a decrease in the tangent Young's modulus with increasing axial compression. From other tests, in which the specimens had a complete instrumentation, we know that the contractancy–dilatancy transition (strain limit state) appears, for this confining pressure, at the same time as the stress peak (stress limit state). Ductile behaviours, combined with a slight softening, are also visible during the post-peak phase of the test.

Each loading–unloading cycle provides the axial elastic stiffness defined by the mean slope of the unloaded deviatoric part. The damage commonly characterised by a decrease in this axial elastic stiffness is not observable before the peak. After the peak, the slope decrease remains limited due to the inhibition created by confinement, whereas the hydrostatic part of the unloading highlights this damage through strong nonlinearity. Such a deviatoric response contrasts with that observed for uniaxial compression test, for which the axial elastic stiffness decreases very quickly once the peak is reached. More information about the evolution of the elastic parameters for different confining pressure are presented in Poinard et al. (2010).

Four scans were performed to study the mesostructural evolution of the R50 specimen. The observations of CT images do not reveal any mesostructural evolution, except for the last cycle leading to failure (Figures 19 and 20). The mesostructure of concrete appears to be undamaged after the two first cycles and even the quantitative measurements do not indicate any significant change. Both entrapped porosity and diameter in the X-direction do not show any modifications (Figure 21). The size distribution presents a slight drop in the most prevalent pores during the second cycle. On the other hand, it is interesting to note the localisation of damage in the last cycle. At the top part

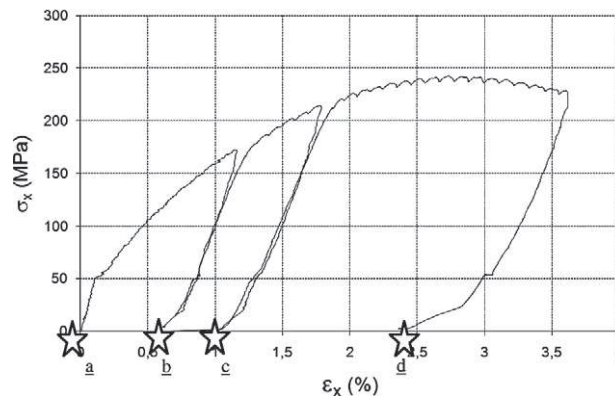


Figure 18. Axial behaviour of R50 specimen under triaxial test at 50 MPa of confining pressure with scans: (a) undamaged; and (b), (c), (d) after each cycle.

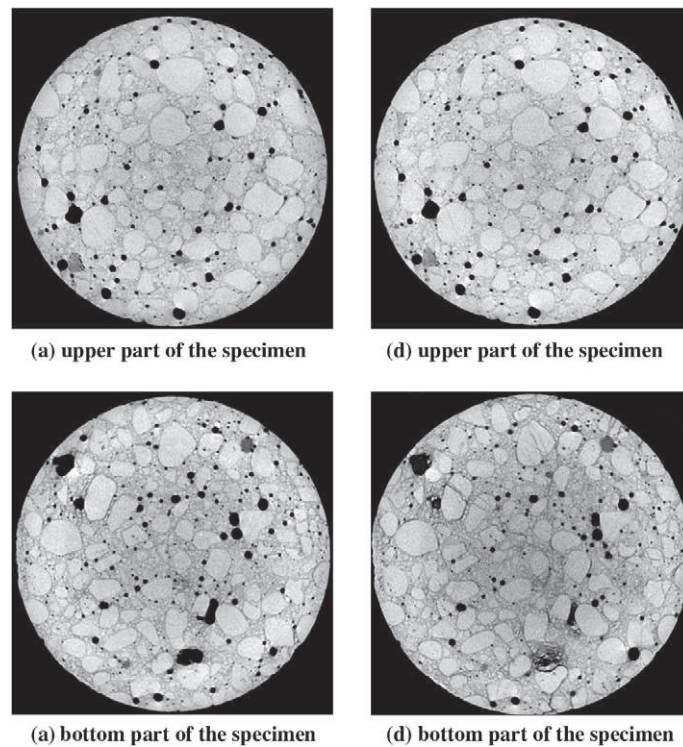


Figure 19. Horizontal slice of R50 specimen after triaxial loading cycles at 50 MPa of confinement: (a) undamaged and (d) after the last cycle. CT scans after cycles (b) and (c) are not shown on this figure.

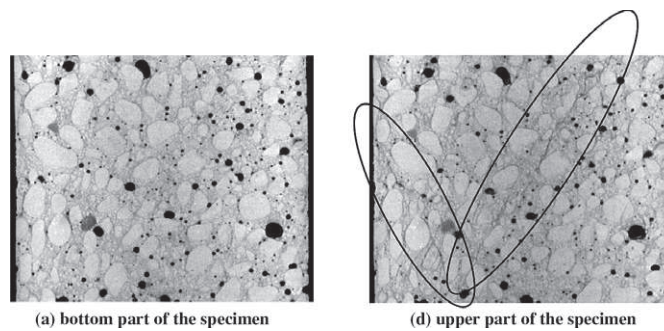


Figure 20. Vertical slice over the lower part of R50 specimen: (a) undamaged; (d) after the last cycle. CT scans after cycles (b) and (c) are not shown on this figure.

of the specimen (Figure 19(d), upper part of the specimen), the mesostructure appears to be undamaged whereas damage is clearly visible over the bottom part (Figure 19(d), bottom part of the specimen). The diameter increases sharply and entrapped porosity

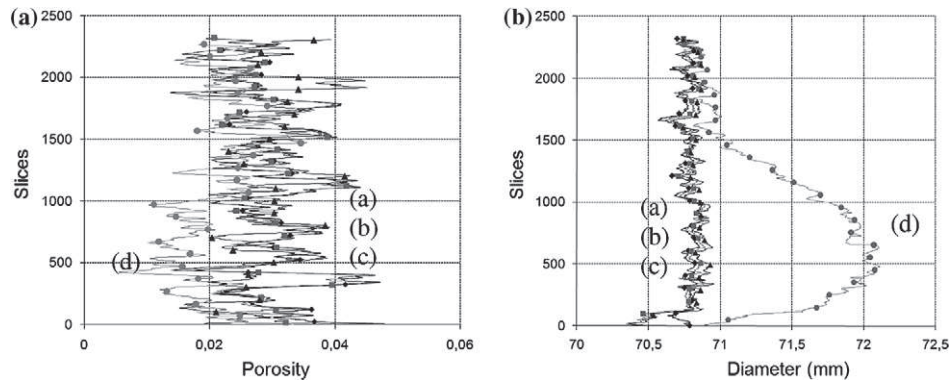


Figure 21. Porosity and diameter of the R50 specimen after increasing triaxial loading cycles at 50 MPa of confinement: ♦ undamaged; ■ after the first cycle; ▲ after the second cycle; and ● after the third cycle. (a) Entrapped porosity in the X-direction; (b) diameter in the X-direction.

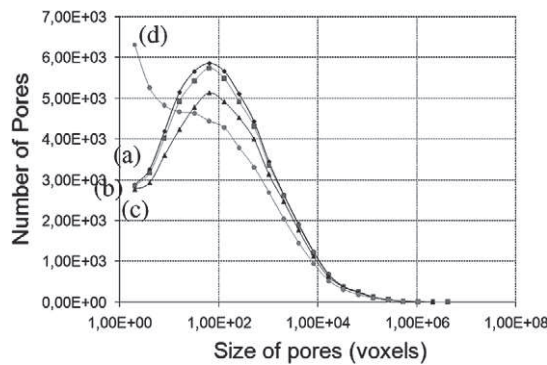


Figure 22. Size distribution of entrapped porosity of R50 specimen with triaxial loading cycles at 50 MPa of confinement: ♦ undamaged; ■ after the first cycle; ▲ after the second cycle; and ● after the third cycle.

decreases (Figures 21 and 22); this behaviour is due to the localisation of damage mechanisms within a specific zone at the time of axial compression.

Figures 19(d) and 20(d) (upper part of the specimen), both exhibit a thin primary crack angled at 60° crossing over specimen R50 without avoiding the aggregates. This feature offers an additional point of divergence with the triaxial compression test at very high confining pressure. The observation of CT images indicates that other inclined cracks exist close to this primary crack. The tilt of these cracks suggests that rupture is due to shear stresses created by axial compression. Figure 23 shows an interesting comparison between the drop in entrapped porosity and inelastic volumetric strain. During the first cycle, the two values match. The second cycle then leads to a higher inelastic volumetric strain stemming from the microstructural modification. The last cycle is noteworthy: a strong decline in entrapped porosity while the inelastic volumetric strain remains nearly stable. This phenomenon is explained by the growth of thin cracks at the microscale leading to dilative behaviour.

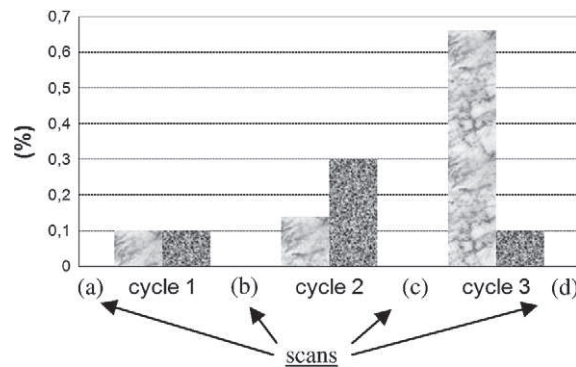


Figure 23. Comparison between the incremental increase in inelastic volumetric strain and the incremental drop in entrapped porosity with triaxial loading cycles at 50 MPa of confining pressure.

The results drawn from the C50 specimens have not been presented yet indicate the same features as for the R50 specimen: the damage mechanisms leading to failure are highly localised, and cracks appear inclined at 60°.

5. Conclusion

This paper has highlighted the role of concrete mesostructure under extreme triaxial compression loadings with a focus on the damage mechanisms created. The experimental campaign consisted of performing CT scans of undamaged specimens and subsequent scans after each loading–unloading cycle with increasing intensity. The obtained CT images enable evaluation of the damage at the mesoscale by means of observations or quantitative measurements, and thus association of it to the macroscopic behaviour.

As expected, the triaxial damage of concrete is highly dependent on the confining pressure attained during the hydrostatic phase. For confining pressures above 400 MPa, the compaction of concrete is significant. Signs of damage, such as collapse of the biggest entrapped porosity or unbonded aggregates, reveal that under very high hydrostatic loading, the strain state is very inhomogeneous at the mesoscopic scale. It was not expected that this phenomenon would mainly be due to macroporosity heterogeneity rather than to the one of the largest aggregates.

For triaxial tests at low confining pressure (around 50 MPa), the cement paste remains very cohesive after the hydrostatic phase. The application of shear loading then creates a localised damage mechanism, which causes specimen failure on a sliding plane inclined at 60°. This mechanism appears and is quantified at the mesoscale once the specimen is failed, which means when the stress peak is reached on the macroscopic stress–strain curve. Outside the failure zone, the concrete remains undamaged at the mesoscopic scale.

For triaxial tests at high confining pressures, observation of the CT images and quantitative measurements show the cement paste loses most of its cohesion during the hydrostatic phase due mainly to entrapped porosity collapse. This phenomenon makes the concrete behave like a non-cohesive granular stacking during the subsequent axial compression and so allows for strong compaction of the concrete specimen before reaching the limit states. In addition, on the CT images, plenty of damage signs appear in both cement paste and aggregates, the compaction is also very visible although there is a decrease in porosity and increase in inelastic volumetric strain. Axial compression under

such a confining pressure reaches a maximum compaction state, which in turn leads to extensive granular rearrangement and hence to dilative behaviour. Beyond this limit state, the rearrangement is so pronounced that one or two cracks almost perpendicular to the axial direction appear at the time of unloading. The horizontal crack opens during hydrostatic unloading, leading to a strong decrease of the bulk modulus of the specimen.

Acknowledgements

The GIGA press was installed in the 3S-R Laboratory within the scope of a cooperative agreement signed with the French Defence Ministry's Armament Division. This research has been performed with the financial support of the Gramat Research Center (CEG, DGA). We would also like to thank Dr Eric Buzaud (CEG) and Dr Christophe Pontiroli for their sound technical and scientific advice.

References

- Bay, B.K., Smith, T.S., Fyhrie, D.P., & Saad, M. (1999). Digital volume correlation: three-dimensional strain mapping using X-ray tomography. *Experimental Mechanics*, 39, 217–226.
- Bentz, D.P., Quenard, D.A., Kunzel, H.M., Baruchel, J., Peyrin, F., Martys, N.S., & Garboczi, E.J. (2000). Microstructure and transport properties of porous building materials. II: Three-dimensional X-ray tomographic studies. *Materials and Structures*, 33, 147–153.
- Besuelle, P. (2004). X-ray CT observations of strain localization and failure in two porous sandstones. In J. Otani J & Y. Obara (Eds.), *X-RAY CT FOR GEOMATERIALS SOILS, CONCRETE, ROCKS* (pp. 287–292).
- Charalampidou, E.M., Hall, S.A., Stanchits, S., Lewis, H., & Viggiani, G. (2011). Characterization of shear and compaction bands in a porous sandstone deformed under triaxial compression. *Tectonophysics*, 503, 8–17.
- Dupray, F., Malecot, Y., Daudeville, L., & Buzaud, E. (2009). A mesoscopic model for the behaviour of concrete under high confinement. *International Journal for Numerical and Analytical Methods in Geomechanics*, 33, 1407–1423.
- Gabet, T., Malecot, Y., & Daudeville, L. (2008). Triaxial behavior of concrete under high stresses: Influence of the loading path on compaction and limit states. *Cement and Concrete Research*, 38, 403–412.
- Gabet, T., Vu, X.H., Malecot, Y., & Daudeville, L. (2006). A new experimental technique for the analysis of concrete under high triaxial loading. *Journal de Physique IV*(134), 635–644.
- Hall, S.A., Bornert, M., Desrues, J., Pannier, Y., Lenoir, N., Viggiani, G., & Besuelle, P. (2010). Discrete and continuum analysis of localised deformation in sand using X-ray μ CT and volumetric digital image correlation. *Geotechnique*, 60, 315–322.
- Landis, E.N., Zhang, T., Nagy, E.N., Nagy, G., & Franklin, W.R. (2007). Cracking, damage and fracture in four dimensions. *Materials and Structures*, 40, 357–364.
- Limodin, N., Rethore, J., Adrien, J., Buffiere, J.-Y., Hild, F., & Roux, S. (2011). Analysis and Artifact Correction for Volume Correlation Measurements Using Tomographic Images from a Laboratory X-ray Source. *Experimental Mechanics*, 51, 959–970.
- Malecot, Y., Daudeville, L., Dupray, F., Poinard, C., & Buzaud, E. (2010). Strength and damage of concrete under high triaxial loading. *European Journal of Environmental and Civil Engineering*, 14, 777–803.
- Poinard, C., Malecot, Y., & Daudeville, L. (2010). Damage of concrete in a very high stress state: Experimental investigation. *Materials and Structures*, 43, 15–29.
- Schmidt, M.J., Cazacu, O., & Green, M.L. (2009). Experimental and theoretical investigation of the high-pressure behavior of concrete. *International Journal for Numerical and Analytical Methods in Geomechanics*, 33, 1–23.
- Sfer, D., Carol, I., Gettu, R., & Etse, G. (2002). Study of the behaviour of concrete under triaxial compression. *Journal of Engineering Mechanics*, 128, 156–163.
- Vu, X.H., Malecot, Y., Daudeville, L., & Buzaud, E. (2009a). Experimental analysis of concrete behavior under high confinement: Effect of the saturation ratio. *International Journal of Solids and Structures*, 46, 1105–1120.

- Vu, X.H., Malecot, Y., Daudeville, L., & Buzaud, E. (2009b). Effect of the water/cement ratio on concrete behavior under extreme loading. *International Journal for Numerical and Analytical Methods in Geomechanics*, 33, 1867–1888.
- Vu, X.H., Malecot, Y., & Daudeville, L. (2009). Strain measurements on porous concrete samples for triaxial compression and extension tests under very high confinement. *Journal of Strain Analysis for Engineering Design*, 44, 633–657.
- Vu, X.H., Daudeville, L., & Malecot, Y. (2011). Effect of coarse aggregate size and cement paste volume on concrete behavior under high triaxial compression loading. *Construction and Building Materials*, 25, 3941–3949.
- Werner, A.M., & Lange, D.A. (1999). Quantitative image analysis of masonry mortar microstructure. *Journal of Computing in Civil Engineering*, 13, 110–115.
- Wong, R.C.K., & Chau, K.T. (2005). Estimation of air void and aggregate spatial distributions in concrete under compression using computer tomography scanning. *Cement and Concrete Research*, 35, 1566–1576.
- Yang, R., & Buenfeld, N.R. (2001). Binary segmentation of aggregate in SEM image analysis of concrete. *Cement and Concrete Research*, 31, 437, 441.
- Zukas, J.A., Nicholas, T., Greszczuk, L.B., Swift, H.F., & Curran, D.R. (1992). *Impact Dynamics*. New York: Wiley.